Predicting magnetospheric dynamics with a coupled sun-to-Earth model: challenges and first results

SPACE WEATHER, VOL. 5, S12001, doi:10.1029/2007SW000335, 2007

Predicting magnetospheric dynamics with a coupled Sun-to-Earth model: Challenges and first results

V. G. Merkin,[1] M. J. Owens,[1] H. E. Spence,[1] W. J. Hughes,[1] and J. M. Quinn[1]

Received 11 May 2007; revised 9 August 2007; accepted 12 August 2007; published 8 December 2007.

[1] Results from the first Sun-to-Earth coupled numerical model developed at the Center for Integrated Space Weather Modeling are presented. The model simulates physical processes occurring in space spanning from the corona of the Sun to the Earth's ionosphere, and it represents the first step toward creating a physics-based numerical tool for predicting space weather conditions in the near-Earth environment. Two 6- to 7-d intervals, representing different heliospheric conditions in terms of the three-dimensional configuration of the heliospheric current sheet, are chosen for simulations. These conditions lead to drastically different responses of the simulated magnetosphere-ionosphere system, emphasizing, on the one hand, challenges one encounters in building such forecasting tools, and on the other hand, emphasizing successes that can already be achieved even at this initial stage of Sun-to-Earth modeling.

Citation: Merkin, V. G., M. J. Owens, H. E. Spence, W. J. Hughes, and J. M. Quinn (2007), Predicting magnetospheric dynamics with a coupled Sun-to-Earth model: Challenges and first results, *Space Weather*, *5*, S12001, doi:10.1029/2007SW000335.

1. Introduction

[2] The main objective of the Center for Integrated Space Weather Modeling (CISM) is formulated in its strategic plan (http://bu.edu/cism/Publications/StrategicPlan.pdf): ''The overarching goal of CISM is to develop a reliable well-validated, comprehensive, physics-based, numerical simulation model that describes the space environment from the Sun to the Earth.'' Building such models is not only important for advancing our understanding of the physics of the Sun-Earth system but also for the development of forecasting tools for the near-Earth space environment. In this paper it is demonstrated that despite challenges we face en route to creating a fully coupled end-to-end model, it is already possible to reproduce some gross features of the dynamics of the magnetosphere-ionosphere system, provided that favorable conditions for such modeling exist in the solar wind.

[3] The complexity of the task at hand is determined partly by the fact that the temporal and spatial scales of physical processes, occurring in different parts of this immense system, sometimes differ by orders of magnitude. For example, the typical density of the solar wind plasma is on the order of $1-10$ cm^{-3}, while the ionospheric plasma is 10^5-10^6 times as dense. Combined with typical plasma temperatures, $T \sim 10^3$ K in the ionosphere and $T \sim 10^4$ K in the solar wind, these numbers yield the typical Debye length of 0.1 cm for the ionospheric plasma and 10^2-10^3 greater in the solar wind [e.g., *Bittencourt*, 2004]. One of the consequences of this great disparity in spatial and temporal scales is that in different regions, different approximations need be used to properly describe plasma behavior. For instance, the ideal magnetohydrodynamic (MHD) treatment is sufficient in many parts of the Earth's magnetosphere and the solar wind but, as is well known, is not applicable in other domains such as the inner magnetosphere and ionosphere.

[4] The first end-to-end model developed at CISM by aggregate efforts of different contributing groups is the CISM 1.0 model, three major components of which are simulation codes based on ideal MHD formalism. The MHD Around a Sphere (MAS) model of the solar corona describes physical processes occurring from the base of the corona out to a radius where the solar wind is supersonic and super-Alfvénic [*Mikic and Linker*, 1994; *Mikic et al.*, 1999; *Linker et al.*, 1999; *Lionello et al.*, 2001; *Riley et al.*, 2001]. The ENLIL model describes the supersonic solar wind plasma flow and fields [*Odstrcil*, 2003], and the Lyon-Fedder-Mobarry (LFM) is a global MHD model of the Earth's magnetosphere [*Fedder and Lyon*, 1995; *Fedder et al.*, 1995a; *Lyon et al.*, 2004], which describes the geospace plasma and fields from upstream of the bow shock to about 300 R_E downtail, where the flow is once again supersonic. In addition, the last model in the chain is the thermosphere-ionosphere nested grid (TING) model

[1]Center for Space Physics, Boston University, Boston, Massachusetts, USA.

which can be coupled to the LFM model to form a two-way fully coupled model of the magnetosphere-ionosphere, the coupled magnetosphere-ionosphere-thermosphere (CMIT) model [*Wang et al.*, 2004; *Wiltberger et al.*, 2004]. The MAS and ENLIL simulation codes can also be combined into a coupled model of the solar corona and solar wind, CORHEL model [*Luhmann et al.*, 2004; *Odstrcil et al.*, 2004]. The LFM model can use as the upstream boundary condition either in situ observations of the solar wind from spacecraft (i.e., ACE or Wind) or, as a component of the CISM 1.0 model, the output from the CORHEL model.

[5] An example of a complication arising from the large differences in spatial and temporal scales of physical processes simulated by the models described is the fact that the entire LFM simulation grid has the size on the order of $\sim 1-2$ cells of the ENLIL grid. This is not necessarily a fundamental weakness, since the simulation resolution is limited largely by the computational cost, but it does pose a serious problem for validation of a model such as CISM 1.0 that covers such diverse physical processes and regions. For instance, the time and location of the heliospheric current sheet (HCS) crossing and the direction of the HCS normal are often used for validation of heliospheric models [*Burton et al.*, 1994; *Owens et al.*, 2005]. However, simulation data that are in good agreement with an L1 monitor on temporal and spatial scales appropriate for a heliospheric model may provide a mediocre input to a magnetosphere-ionosphere model because most of the small-scale features, i.e., interplanetary magnetic field (IMF) B_z variations, crucial for an accurate description of the magnetospheric dynamics, will be missed. Another complication follows from the fact that physical models of the solar corona are presently bound to be time-independent, as their inner boundary conditions are synoptic magnetograms, and to obtain such an observation for the entire surface of the Sun, a full Carrington rotation (CR), i.e., 27.27 d, has to pass. The lack of time-dependent structures, such as coronal mass ejections (CMEs), in the initial coupled model of the solar corona and the heliosphere poses a critical problem for the magnetosphere-ionosphere modeling.

[6] In this paper we present results of CISM 1.0 simulations of two 6- to 7-d intervals belonging to two different Carrington rotations. These intervals represent two different HCS configurations that are reproduced reasonably well by the CORHEL model but lead to different responses of the global magnetospheric model driven by the CORHEL output. During the first interval, CORHEL captured the global structure of the HCS, but owing to the flatness of the HCS, no current sheet crossing occurred in the virtual L1 monitor, which resulted in very weak variability in the data that were actually input into the CMIT 1.0 model. During the second interval, the HCS exhibited a distinct three-dimensional structure captured by the CORHEL simulation fairly well. In this case the virtual L1 monitor observed an HCS crossing yielding a time-dependent solar wind input into the magnetospheric model. Neither of the intervals, however, revealed a southward B_z component sufficient to stimulate significant magnetospheric activity. Despite this crucial deficiency, i.e., B_z variations being essentially subgrid phenomena in present solar wind models, it is demonstrated in this paper that under favorable conditions (i.e., B_y-driven periods, provided that the IMF B_y component is captured well by the heliospheric model), large-scale signatures of magnetospheric dynamics can already be reproduced.

[7] We use the cross–polar cap potential as a global indicator of magnetospheric activity for our analysis. This quantity, defined as the difference between the maximum and the minimum electrostatic potential associated with the ionospheric convection pattern, is a good descriptor of the magnetospheric convection pattern as well, owing to the notion of the former being a footprint of the latter in an average sense. During the first interval, we investigate the dynamics of the magnetosphere using the stand-alone LFM model and the CMIT 1.0 model driven by the Wind solar wind observations, as well as the CISM 1.0 model, and contrast the results of these three models to one another and to the baseline model, Weimer'05 [*Weimer*, 2005a, 2005b]. The second interval is simulated by the stand-alone LFM model and the CISM 1.0 model only, where in the case of the CISM 1.0 model, LFM is not coupled to TING, and the ionospheric conductances are calculated empirically. In the simulations of this interval we are interested in investigating the magnetospheric response to the HCS configuration different from the one during the first interval (three-dimensional versus flat) and contrasting the two. Furthermore, the time-dependent output of the heliospheric model in this case allowed for a more sensible comparison of the simulation results of the LFM model driven by the CORHEL output and upstream observations.

[8] In section 2 we provide a brief summary of each component of the CISM 1.0 model. Section 3 discusses results of heliospheric simulations of the two Carrington rotations and their comparisons with L1 observations. In section 4 we present results of global magnetospheric simulations of the cross–polar cap potential evolution. Section 5 concludes the paper.

2. CISM 1.0 Simulation Model

[9] Each of the models constituting the CISM 1.0 model has been extensively used for investigations of its own physical domain. Ample literature exists describing the numerics of these models and their physical results. Therefore we do not attempt to provide an exhaustive description of every model here but rather make a brief introduction providing the interested reader with corresponding references.

2.1. MAS Model

[10] The global corona is modeled by the Magnetohydrodynamics Around a Sphere (MAS) three-dimensional

(3-D) MHD simulation code developed by the Science Applications International Corporation group [*Linker et al.*, 1999; *Mikic et al.*, 1999] (see also http://imhd.net). Photospheric magnetic field observations from the National Solar Observatory at Kitt Peak (www.synoptic.nso.edu) provide the boundary conditions, from which initial conditions are derived by a potential field solution to the photospheric radial field, a uniform boundary density, and a Parker-type solar wind outflow. The time-dependent MHD equations, with finite resistivity and viscosity, are then solved in spherical geometry between 1 and 30 R_S using a polytropic index of $\gamma = 1.05$ to approximate the near-isothermal nature of the corona (see *Mikic and Linker* [1994] for details of the code numerics). The solution is allowed to relax to steady state conditions.

[11] The polytropic approach, taken for both physical simplicity and computational reasons, does not yield sufficient variation in the plasma parameters. More complex treatments of the energy equation should result in more realistic thermodynamics [*Lionello et al.*, 2001], though such methods have yet to be fully refined. However, we note that the flow at the polytropic MAS outer boundary is still supercritical, greatly simplifying the coupling to the coronal code.

2.2. ENLIL Model

[12] The heliosphere is modeled by the ENLIL 3-D ideal MHD code developed at the University of Colorado [e.g., *Odstrcil*, 2003, and references therein]. As with MAS, a polytropic energy equation is used but with the observationally derived value of $\gamma = 1.5$ [*Toten et al.*, 1995]. The computational domain covers 30 R_S to 1 AU and -60° to $+60^\circ$ in solar latitude.

[13] Boundary conditions are provided by the MAS coronal solution (see *Odstrcil et al.* [2004] and *Luhmann et al.* [2004] for details of the code coupling). The radial component of the magnetic field (B_R) computed by MAS is used directly, whereas the meridional component (B_θ) is assumed to be zero, and the azimuthal component (B_φ) is derived from the rotation speed of the source surface (i.e., $B_\varphi = -B_R(V_{\mathrm{ROT}}/V_R)\sin\theta$, where V_R is the radial flow speed and V_{ROT} comes from the 27.27-d rotation period of the Sun). Because of insufficient variability in the MAS plasma parameters caused by the polytropic approximation, an empirical relation, based upon the well-determined magnetic topology of the coronal solution, is used to specify the radial plasma flow speed [*Riley et al.*, 2001]. The nonradial components of the plasma flow are assumed to be zero on the ENLIL inner boundary, whereas density and temperature are specified from the assumptions of constant momentum flux and thermal pressure balance, respectively. The heliospheric solution is allowed to relax to steady state.

[14] For this initial Sun-to-Earth validation study we use the computationally efficient versions of the codes: MAS (ENLIL) has 60, 70, and 64 (128, 30, and 90) grid cells in the radial, meridional, and azimuthal directions, respectively.

2.3. LFM Model

[15] The Lyon-Fedder-Mobarry global MHD model simulates the Earth's magnetosphere by solving ideal MHD equations on a 3-D distorted spherical grid with the symmetry axis aligned with the solar magnetic (SM) x axis [*Lyon et al.*, 2004, and references therein]. The grid is contained in a cylindrical volume with the radius of $\sim$100 R_E, the front boundary placed at $\sim$30 R_E and the back boundary at $\sim$300 R_E. For the present study the lowest-resolution LFM simulation grid is used with 53 cells in the radial direction and 24 and 32 cells in the polar and azimuthal directions (in the LFM sense), respectively. The resolution in the radial direction defines the location of the inner boundary of the MHD grid at $\sim$2 R_E, which places the low-latitude ionospheric boundary at $\sim 45^\circ$ magnetic latitude.

[16] The inner boundary condition of the LFM model follows from the electrostatic, thin shell approximation of the ionosphere whereby the current continuity condition relates the electrostatic potential to the field-aligned current through the height-integrated ionospheric conductivity [*Fedder and Lyon*, 1995; *Fedder et al.*, 1995a; *Lyon et al.*, 2004]. Conventionally, the ionospheric conductance is calculated by an empirical model which first computes the EUV ionization contribution and then estimates the precipitating particle characteristic energy and flux from MHD macrovariables [*Fedder et al.*, 1995b]. The latter are then transferred into the ionospheric conductance according to Robinson's formulae [*Robinson et al.*, 1987]. In the CMIT 1.0 model [*Wiltberger et al.*, 2004; *Wang et al.*, 2004] the LFM is coupled to the thermosphere-ionosphere nested grid model [*Wang et al.*, 1999] that replaces the empirical calculation of the ionospheric conductances in the stand-alone LFM.

2.4. TING Model

[17] The thermosphere-ionosphere nested grid model [*Wang et al.*, 1999] is an extension of the National Center for Atmospheric Research (NCAR) coupled thermosphere-ionosphere global circulation model [*Roble et al.*, 1988, and references therein] with high-resolution capabilities. The model solves for the hydrodynamics and thermodynamics of neutral and ionized species coupled both dynamically and chemically. Ionized components are driven, in addition to gravity, pressure gradients, and ion-neutral collisions, by the $\mathbf{E} \times \mathbf{B}$ term. In stand-alone model runs, the convective electric field is usually obtained from an empirical model of the ionospheric convection, whereas in the LFM-coupled mode (CMIT) it is provided by the LFM ionospheric boundary condition [*Wang et al.*, 2004; *Wiltberger et al.*, 2004]. Particle precipitation parameters (characteristic energy and flux) computed empirically in the LFM are also put into the TING calculation. The ionospheric conductance is one of the outputs of the TING

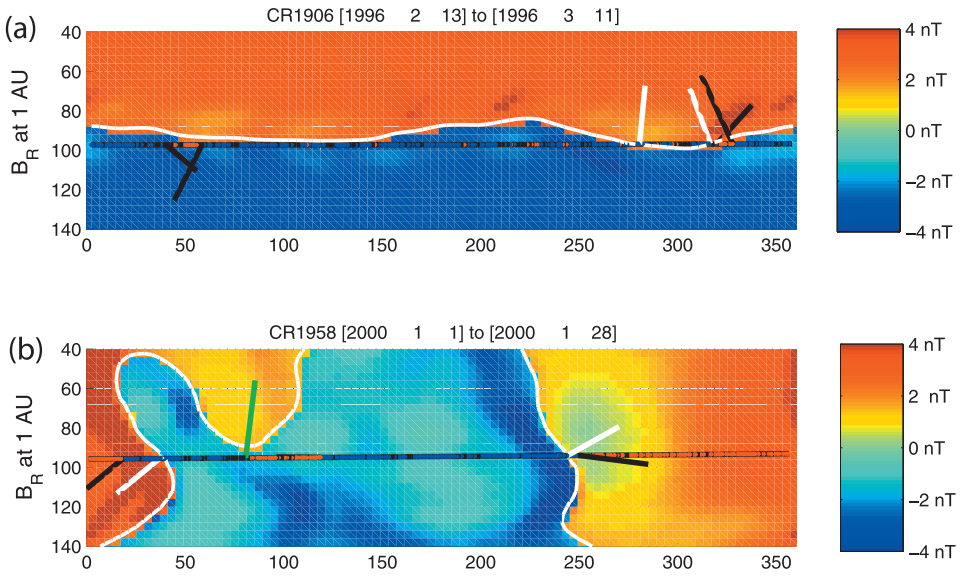

Figure 1. Carrington map of CORHEL-computed radial field and associated heliospheric current sheet at 1 AU (white curve) on a heliocentric surface of R = 215 R_S. Red (blue) shows outward (inward) polarity. White lines show the predicted HCS normals for Earth crossings. Overlaid on the model output are the observed magnetic sectors (same color code; black regions are of indeterminate sector) and HCS orientations (black lines) at L1. Green lines show HCS crossings associated with ICMEs. Maps show Carrington rotation for (top) 1906 and (bottom) 1958.

model and, as mentioned above, in the CMIT model it is used for the LFM inner boundary specification instead of empirical values.

3. CORHEL Comparisons at the L1 Point

3.1. Observation Techniques

[18] Solar wind observations at the L1 point are obtained from the Goddard Space Flight Center Space Physics Data Facility OMNIWeb interface at http://omniweb.gsfc.nasa.gov. For computation of sector structure and HCS inclination we average this data to 5-min resolution. Inward (outward) sectors are defined as periods of solar wind with the magnetic field vector within 30° of the positive (negative) ideal Parker spiral angle. Periods that fail to meet either the inward or outward criteria are classified as unknown sectors. To reduce small-scale effects, HCS crossings are classified as changes in polarity with a minimum of 30 min of continuous polarity on either side of the inversion.

[19] The orientation of the observed HCS crossings is determined using minimum variance analysis (MVA) [*Burton et al.*, 1994]. We note that typically, the error in using MVA to estimate the orientation of discontinuities is <10° [*Lepping and Behannon*, 1980]. As the derived orientation can be sensitive to the choice of duration on either side of the polarity inversion, we calculate an ensemble of orientations using a sliding window from half a day to half an hour on either side of the HCS crossing. Each HCS orientation is assigned a "confidence" using the ratio of the intermediate-to-minimum and maximum-to-intermediate eigenvalue ratios. If the maximum confidence HCS orientation is not close to the average HCS orientation over the whole ensemble (e.g., >20°), then the HCS orientation is discarded.

3.2. CR 1906 Simulation

[20] The top plot of Figure 1 shows the observed and modeled magnetic field at 1 AU for CR 1906. The main color map is a Carrington map (i.e., a latitude-longitude slice at fixed radial distance) of the model-computed radial field (red and blue are outward and inward polarity, respectively) and associated heliospheric current sheet (white curve) on a heliocentric surface of R = 1 AU. White lines show the predicted HCS normals for Earth crossings. The position of the L1 point is shown by the thick, near-horizontal black line: As the CORHEL solution is steady state, a time series for a virtual spacecraft at L1 can be generated by moving along this line from right (the start of the CR, 13 February 1996) to left (the end of the CR, 11 March 1996). Overlaid on the L1 path are the L1 observed magnetic sectors (same color code; black regions are of indeterminate sector) and observed HCS orientations (black lines). CORHEL predicts that the IMF polarity at L1 should be primarily inward, as is observed. CORHEL predicts the excursion into outward polarity near the start of the CR (~320° Carrington longitude) later, and for a longer duration, than is observed. The inclinations of the predicted HCS crossings approximately match those observed. The later, shorter excursion into inward polarity

(~50° Carrington longitude) is not predicted by CORHEL at all. As the HCS is so flat, the L1 point skims along the current sheet throughout this entire period, making prediction of the HCS crossings particularly difficult. Indeed, the abundance of observed small-scale sector crossings suggests that the HCS was close to the L1 point for the entire CR, as predicted by CORHEL. This issue is discussed further in section 4.

3.3. CR 1958 Simulation

[21] The bottom plot of Figure 1 shows the observed and modeled magnetic field at 1 AU for CR 1958. CORHEL predicts a two-sector structure, from inward to outward sector, which matches the observations well. The timing and inclination of the first HCS crossing (Carrington longitude 250°) is well captured by CORHEL. The second major HCS crossing (Carrington longitude 20°) is predicted ~1.5 d too early though the orientation is very well matched. We note that there is a short-duration inward polarity excursion from Carrington longitudes 120° to 80° that is missed by CORHEL. However, CORHEL predicts an equatorial extension of inward polarity close to this Carrington longitude, but it does not quite extend all the way down the ecliptic so as to produce HCS crossings at L1. Furthermore, the green line indicates a crossing associated with an interplanetary coronal mass ejection, which may have distorted the magnetic structure of the corona in ways CORHEL is not expected to capture, as the MAS simulation is driven by a synoptic magnetogram and hence does not include transient features such as CMEs.

4. Magnetospheric Dynamics

4.1. CR 1906 Simulation

[22] Figure 2 (red traces) shows the output from the CORHEL model (Figure 1a) when it is put in the form suitable for input into the LFM model: time series of upstream solar wind plasma and magnetic field parameters in the GSE coordinate system. The picture is complemented by the Wind spacecraft data in the same format (black traces). For the magnetospheric part of the simulation we choose the interval from 23 to 29 February 1996 corresponding approximately to the segment extending from 160° to 235° Carrington longitude in Figure 1a. This interval is selected for two reasons. First, we deliberately choose an event with a very simple HCS configuration when, as shown below, the magnetospheric dynamics are driven by small-scale variations in the IMF (mostly southward B_z). Such small-scale IMF drivers are turbulent-like in nature and are beyond the capability of current heliospheric simulation models. Thus while the HCS configuration is simple, the modeling challenge is great. An opposite case is the CR 1958 simulation considered in section 4.2. Second, this 6-d interval was previously examined by *Guild* [2007] in his plasma sheet statistical study using the stand-alone LFM model, and the cross–polar cap potential results for the stand-alone LFM below are extracted from those simulation data. This explains our use of the Wind data to drive the LFM and CMIT 1.0 models (Figure 2, black traces) as those solar wind data were used by *Guild* [2007], in contrast to Figure 1a, where the CORHEL results are compared with the ACE data. The use of Wind (Figure 2) instead of ACE (Figure 1) data does not affect the evident conclusion that when reduced to a single point measurement (and therefore concentrating on small-scale features), the CORHEL simulation data for this interval yield poor agreement with the spacecraft observations. In the absence of CMEs in the heliospheric model or corotating interaction regions (CIRs) during the simulated interval, a large-scale time-dependent structure in the CORHEL output at L1 can be expected if an HCS crossing occurs. During this period, there appears to have been a number of small HCS crossings. This is supported by the CORHEL simulation which predicts the L1 point to skim the HCS at this time. However, partly because of the coarse nature of the simulation, the virtual L1 point never crosses the HCS, resulting in the marked difference between the virtual and observed L1 time series. A situation when an HCS crossing did occur in the CORHEL simulation is considered in section 4.2., while here we note that a more subtle problem, common to both CR 1906 and CR 1958 simulations, is the lack of small-scale structures responsible for IMF B_z variations, since these structures are essentially subgrid phenomena in the CORHEL model. These small-scale (from the point of view of the heliospheric model) variations are the most important drivers of the magnetospheric dynamics in the absence of large-scale time-dependent structures, such as CMEs, CIRs, or HCS crossings.

[23] *Spence et al.* [2004] define several metrics for quantitative assessment of CISM models. Here we employ the cross–polar cap potential as a top-level metric for validation of the geospace segment of the CISM 1.0 model. The time evolution of this parameter, quantifying the strength of the solar wind–magnetosphere–ionosphere interaction and calculated by the indicated models, is demonstrated in Figure 3. The black, yellow, and red traces show the cross–polar cap potential calculated by the CMIT 1.0, stand-alone LFM, and the CISM 1.0 models, respectively. The blue trace represents the potential inferred from the Weimer'05 model [*Weimer*, 2005a, 2005b], which we use as the baseline model for our analysis.

[24] It is instructive to consider the differences and similarities between the time series in Figure 3 one by one. First, the red trace (CISM 1.0 model) demonstrates clearly that during the simulated interval, the magnetospheric dynamics were driven by small-scale variations in the solar wind plasma and magnetic field parameters, in particular the IMF B_z component, which are not captured by the CORHEL model. The large-scale oscillations that the red trace exhibits are due to diurnal variations of the magnetic dipole tilt and are completely dominated by the solar wind and IMF-driven dynamics as the other traces in Figure 3 demonstrate.

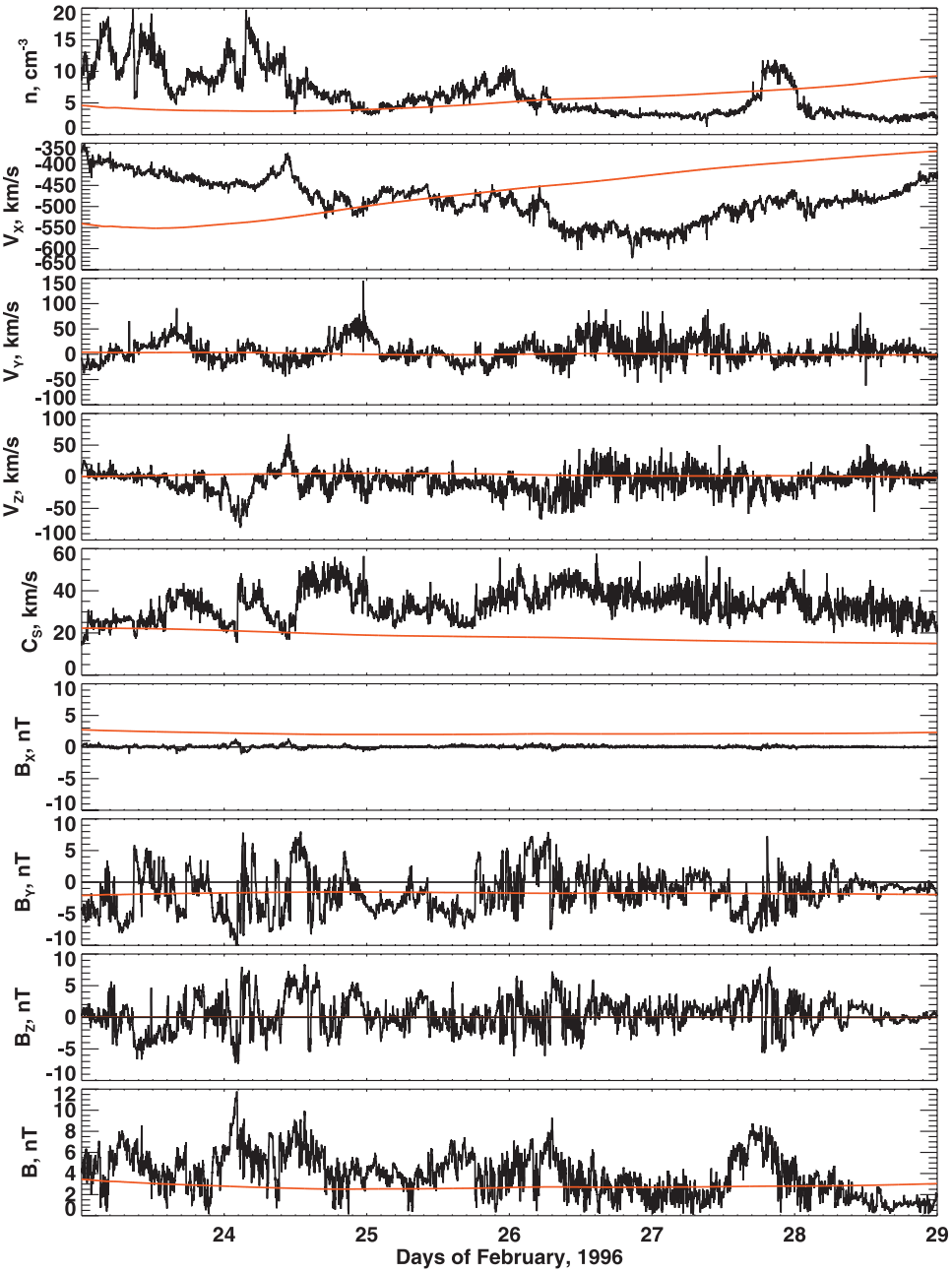

Figure 2. Solar wind parameters in the GSE coordinate system as observed by the Wind spacecraft (black trace) and simulated by the CORHEL model at L1 (red trace) for the CR 1906 interval.

[25] Inspection of the black, yellow, and blue traces in Figure 3 (stand-alone LFM, CMIT 1.0, and Weimer'05 models, respectively, all initiated by the Wind spacecraft solar wind plasma and magnetic field observations) yields that the LFM and CMIT 1.0 time series are well correlated with the Weimer'05 results. This is quantified by the high linear correlation coefficients, 0.93 for LFM/Weimer'05 and 0.90 for CMIT 1.0/Weimer'05, respectively. We note that one should not expect the models to be perfectly correlated. Indeed, the Weimer'05 model uses the solar wind input averaged over 50 min and thus describes a mean, smoothed ionospheric convection pattern, while the global MHD model is capable of reproducing processes occurring on faster time scales. However, considering the

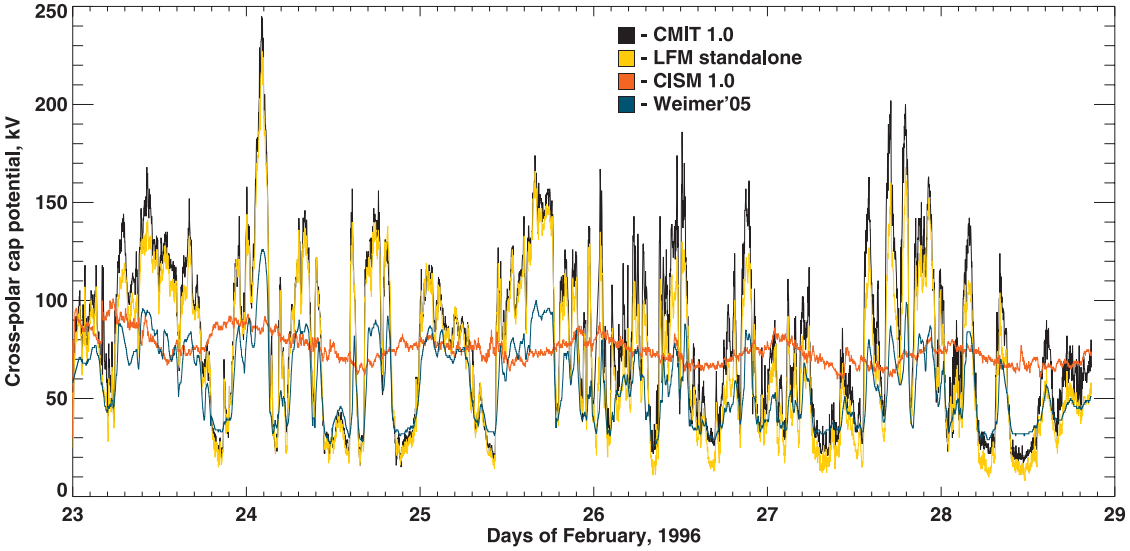

Figure 3. Time evolution of the cross−polar cap potential calculated by the indicated models for the 6-d interval during CR 1906.

high values of the aforementioned correlation coefficients, we conclude that the influence of this factor was minimal during the interval simulated.

[26] Among the quantitative disparities between the LFM and CMIT 1.0 models on one side and the Weimer'05 on the other is the consistent overestimation of the cross−polar cap potential by the former. For this relatively quiet interval, the Weimer'05 model is likely to reproduce the cross−polar cap potential that agrees well with observations (D. R. Weimer, personal communication, 2007). We are currently working on obtaining the Defense Meteorological Satellite Program (DMSP)-inferred values of the potential (our initial analyses do indicate good agreement between the DMSP measurements and the Weimer'05 values) and the results of the corresponding comparisons, and more formal skill-score analysis will be published elsewhere. We do note here that the overestimation of the cross−polar cap potential by the LFM model, as well as other global MHD models, is a well-known effect which has been shown to be somewhat remedied by inclusion of microphysical processes resulting in a higher ionospheric conductance [*Merkin et al.*, 2005] or ionospheric ion outflows [*Winglee et al.*, 2002]. Addressing this matter in general is beyond the scope of this paper and will not be discussed here any further.

4.1.1. Convergence of the Ionospheric Solution

[27] We now turn to the discussion of the comparison between the stand-alone LFM and the CMIT 1.0 model results. As mentioned above, in the CMIT 1.0 simulation, the neutral wind feedback from the TING model was not taken into account in the ionospheric boundary calculation of the LFM model. Therefore the difference between the stand-alone LFM and the CMIT 1.0 model simulations is due only to different values of the ionospheric conductance used. It is in order here to mention a caveat which is perhaps common to all coupled models of thermosphere-ionosphere-magnetosphere, such as the CMIT 1.0 model. The formulation of the inner-boundary condition for a global MHD model involves finding the ionospheric potential in a thin spherical shell approximation:

$$\nabla \cdot (\boldsymbol{\Sigma} \nabla \boldsymbol{\Phi}) = j_{\parallel} \sin \delta, \tag{1}$$

where $\boldsymbol{\Sigma}$ is the height-integrated conductivity tensor, δ is the dip angle, Φ is the ionospheric electrostatic potential, and $j_{\parallel}$ is the field-aligned current density [e.g., *Lyon et al.*, 2004]. The conductance tensor is given by

$$\boldsymbol{\Sigma} = \begin{bmatrix} \Sigma_P / \sin^2 \delta & -\Sigma_H / \sin \delta \\ \Sigma_H / \sin \delta & \Sigma_P \end{bmatrix}. \tag{2}$$

Convergence properties of the numerical solution of equation (1) are dependent on values of the ionospheric conductances, Σ_P (Pedersen) and Σ_H (Hall). When the empirical model is used to calculate Σ_P and Σ_H in the stand-alone LFM model, their values can be modified so as to ensure the convergence of the elliptical solution. This involves setting a lower limit on both the Pedersen and Hall conductances, which is usually set to 2 S in the stand-alone LFM model but can be arbitrary. However, the TING model is not restricted in this sense and can produce conductances that lead to an ill-defined solution matrix. In the interval presented we noticed that the ionospheric solution of the CMIT 1.0 model became unstable at times during the first 3 d of the interval, and we modified Σ_P and Σ_H obtained from the TING model in the manner that is done in stand-alone LFM simulations to ensure the stability of the solution. During the second

half of the interval, the ionospheric calculation was well behaved, and no modifications to the TING conductances were introduced.

[28] There can be a number of reasons for bad convergence of the ionospheric elliptic calculation. One of them is that for certain ratios Σ_H/Σ_P, the equation becomes parabolic or hyperbolic, which entails modifications to the boundary conditions and/or numerical algorithm to obtain the valid solution [*Goodman*, 1995]. According to *Goodman* [1995], the equation is purely elliptic when $1 - \alpha^2 f(\theta) < 0$, where $\alpha = \Sigma_P(\phi, \theta)/\Sigma_H(\phi, \theta)$, $f(\theta) = 16\cos^2\theta(1 + 3\cos^2\theta)/\sin^4(\theta)$, and ϕ and θ are the azimuthal and the polar angles, respectively. The *Goodman* [1995] inequality translates into $\Sigma_H/\Sigma_P < \sqrt{f(\theta)}$, which is true for virtually any realistic ratio of the conductances for locations poleward of the polar cap boundary. Inspecting the ionospheric conductance values obtained from the TING model (not shown here) demonstrates that the condition above was satisfied by a large margin and therefore could not be the cause of the bad convergence of the ionospheric solution.

[29] Furthermore, equation (1) is derived under the assumption that no perpendicular current is flowing in the gap region, the region between the inner boundary of the global MHD simulation (usually placed at 2–3 R_E in the LFM simulation code) and the ionosphere. The neglect of the perpendicular polarization current in the gap region is well justified in the limit $v_c \ll v_A$, where v_c is the characteristic velocity and v_A is the Alfvén speed [*Lotko*, 2004]. In the electrostatic ionosphere approximation, which is likely to hold in the low ionospheric conductance limit discussed here, the characteristic speed can be shown to be approximately inversely proportional to the Pedersen conductance:

$$v_c \approx \frac{c^2}{4\pi\Sigma_P}, \tag{3}$$

and therefore the neglect of the polarization current is justified when $\Sigma_P \gg \Sigma_A$, where $\Sigma_A = c^2/4\pi v_A$ is the Alfvénic impedance. The estimate based on $v_a \approx 2.5 \times 10^6$ m/s at 500 km altitude [*Lotko*, 2004] yields $\Sigma_A \approx 0.3$ S, which is in agreement with the estimate $\Sigma_A < 1$ S given by *Mallinckrodt and Carlson* [1978]. In the simulation discussed here, the conductances obtained from the TING model simulation did go below 1 S owing to the low ionospheric plasma density, so the low Pedersen conductance could have become comparable to the Alfvénic impedance. It is not clear, however, how the breaking down of the approximation in which equation (1) was derived (no polarization currents in the gap region) can result in the nonconvergence of the ionospheric solution since mathematically, the problem remains well defined and will just result in characteristic velocities v_c that are probably unrealistically high.

[30] Another and perhaps the most likely reason for the nonconvergence of the ionospheric equation solution is the combination of low conductances produced by the TING model and the noisy field-aligned currents produced by the LFM model at low latitudes. This noise is partly a result of the LFM ionospheric grid [see *Wiltberger et al.*, 2004, Figure 1], which is the projection of the distorted spherical grid utilized in the LFM simulation code for the magnetospheric solution. Future numerical tests will show whether this factor was really key in determining the convergence properties of the ionospheric solution and if so, what measures should be taken to resolve this issue.

4.1.2. LFM Versus CMIT 1.0

[31] As mentioned above, to make the ionospheric solution well behaved during the first 3 d of the discussed interval, we have applied the lower limit of 2 S to the conductances produced by the TING model (the same threshold was applied to the conductances in the standalone LFM simulation runs by default), which resulted in a converged solution. The fact that the lower limit on the ionospheric conductance was set during the first half of the simulated interval had the result that the peak values of the cross–polar cap potential were much closer between the LFM and CMIT 1.0 models than when this threshold was not set (last 3 d of the simulation). This is demonstrated in Figure 4, where the LFM (yellow dots) and CMIT 1.0 (black squares) cross–polar cap potentials are shown, from which the Weimer'05 values are subtracted. Clearly, the data points above the horizontal blue line correspond to the times when the LFM (CMIT 1.0) model values are higher than the Weimer'05 values, while the data points below that line correspond to the times when these models are below Weimer'05 values. The latter instances are less abundant but are present in the simulation data as well. The fact that there are more data points where the positive (CMIT 1.0 minus Weimer'05) difference is larger than the positive (LFM minus Weimer'05) difference during the second half of the interval than during its first half suggests that during the first 3 d both LFM and CMIT 1.0 models operated close to the conductance threshold and therefore produced similar cross–polar cap potentials. During the second 3 d the CMIT 1.0 conductance was in general smaller than the LFM conductance, as it was not bound from below, which resulted in the overall larger cross–polar cap potentials.

[32] The relatively rare instances when the LFM and CMIT 1.0 potentials are smaller than the Weimer'05 values (data points below the blue horizontal line in Figure 4) occur mostly during the times of weak driving, which is seen in Figure 4 as these points tend to occupy the area to the left on the horizontal axis, where the Weimer'05 potential values are the lowest. The underestimation of the cross–polar cap potential by the LFM model during weak solar wind forcing, especially during northward IMF periods, was shown to be remedied by increasing the simulation resolution [*Merkin et al.*, 2007], which improves both the representation of the high-latitude magnetopause reconnection region of NBZ current system generation

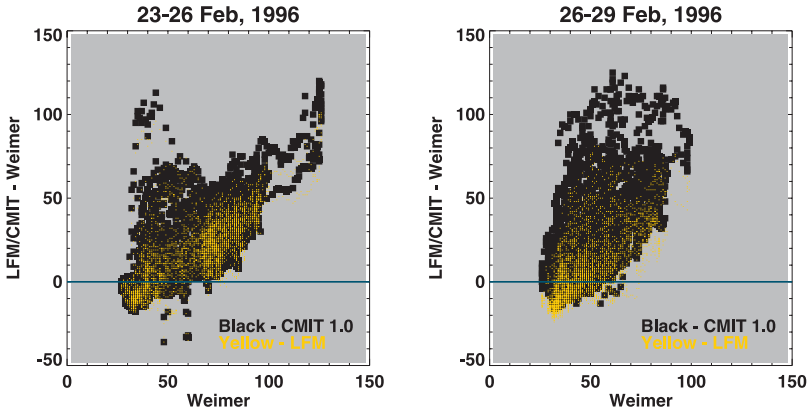

Figure 4. Difference between the LFM (yellow dots) and CMIT 1.0 (black squares) values of the cross–polar cap potential and the Weimer'05 predictions. Shown are simulation data during (left) the first 3 d of the simulated interval (when the lower limit of 2 S on the ionospheric conductances was set) and (right) the last 3 d of the simulated interval (no lower limit on the conductance). Clearly, the data points above the horizontal blue line show the corresponding model's results that are higher than the Weimer'05 value, and the points below the line show results that are smaller than the Weimer'05 value.

and the viscous interaction at the flanks of the magnetopause. The effects of the ionospheric conductance model are minor in this regime for both parts of the simulation, with and without the lower limit on the conductance values (both plots in Figure 4). During the second half of the interval (the right plot in Figure 4) there are a few times when the CMIT 1.0 cross–polar cap potential was higher than the LFM values (and closer to the baseline model values), suggesting the smaller conductance values unbound from below.

4.2. CR 1958 Simulation

[33] For the global magnetospheric simulation during CR 1958 we choose a 7-d (87° in terms of Carrington longitudes) interval surrounding the HCS crossing that occurred at Carrington longitude 250°. Figure 5 shows the CORHEL model output along with the ACE spacecraft data in GSE coordinates as these data are input into the LFM model. In this example simulation we use the conventional LFM model instead of the CMIT 1.0 model for the magnetospheric segment of the simulation. Since we are looking to separate effects of the solar wind and IMF driving from effects of the ionospheric conductance, running the CMIT 1.0 model instead of the LFM is not required.

[34] As discussed above, during this interval, the HCS exhibited a clear three-dimensional structure, and the particular HCS crossing at 250° Carrington longitude was captured well by the CORHEL model. Examining Figure 5 confirms that the large-scale structure of the solar wind flow and solar magnetic field is reproduced much better (cf. Figure 3 for the CR 1906 comparisons). The IMF structure in terms of B_x and B_y is reproduced quite well, considering that the CORHEL data are 1-h averages, while the ACE data are given on a 1-min cadence. The HCS crossing seen in the ACE data approximately at the beginning of the day on 9 January (coincides with the vertical line 1) is predicted by the CORHEL model but about 0.5 d later (seen as small jumps in B_x and B_y components of the magnetic field). This half-day shift corresponds to an error in the position of HCS on the scale of just one CORHEL grid cell, but it is, of course, crucial for driving the global MHD model. Because of this shift, the cross–polar cap potential response to B_z and especially B_y turning seen between the vertical lines 1 and 2 in Figure 5j (black trace) is missed completely by the LFM model driven by the CORHEL input (red trace). However, later in the day of 9 January and a part of 10 January (between the vertical lines 2 and 3), CORHEL captures very well the trend of B_y, which appears to be the main driver of activity during this period. This is confirmed by inspection of the northern hemisphere convection patterns simulated by the LFM model driven by both the ACE spacecraft observations and the CORHEL model output. Figure 6 demonstrates snapshots of these patterns taken at the peak of the B_y-driven interval at 0000 UT on 10 January. The two convection patterns are remarkably similar and look very much like the classical negative B_y-driven convection pattern in the winter hemisphere [e.g., *Rich and Hairston*, 1994; *Haaland et al.*, 2007]. Turning back to Figure 5 we note that following the very well captured period between vertical lines 2 and 3, B_z turned southward for the rest of the day on 11 January. This southward excursion of IMF B_z was not predicted by the CORHEL model and therefore did not lead to the appropriate response of the cross–polar cap potential simulated by the LFM model (the interval between the vertical lines 3 and 4).

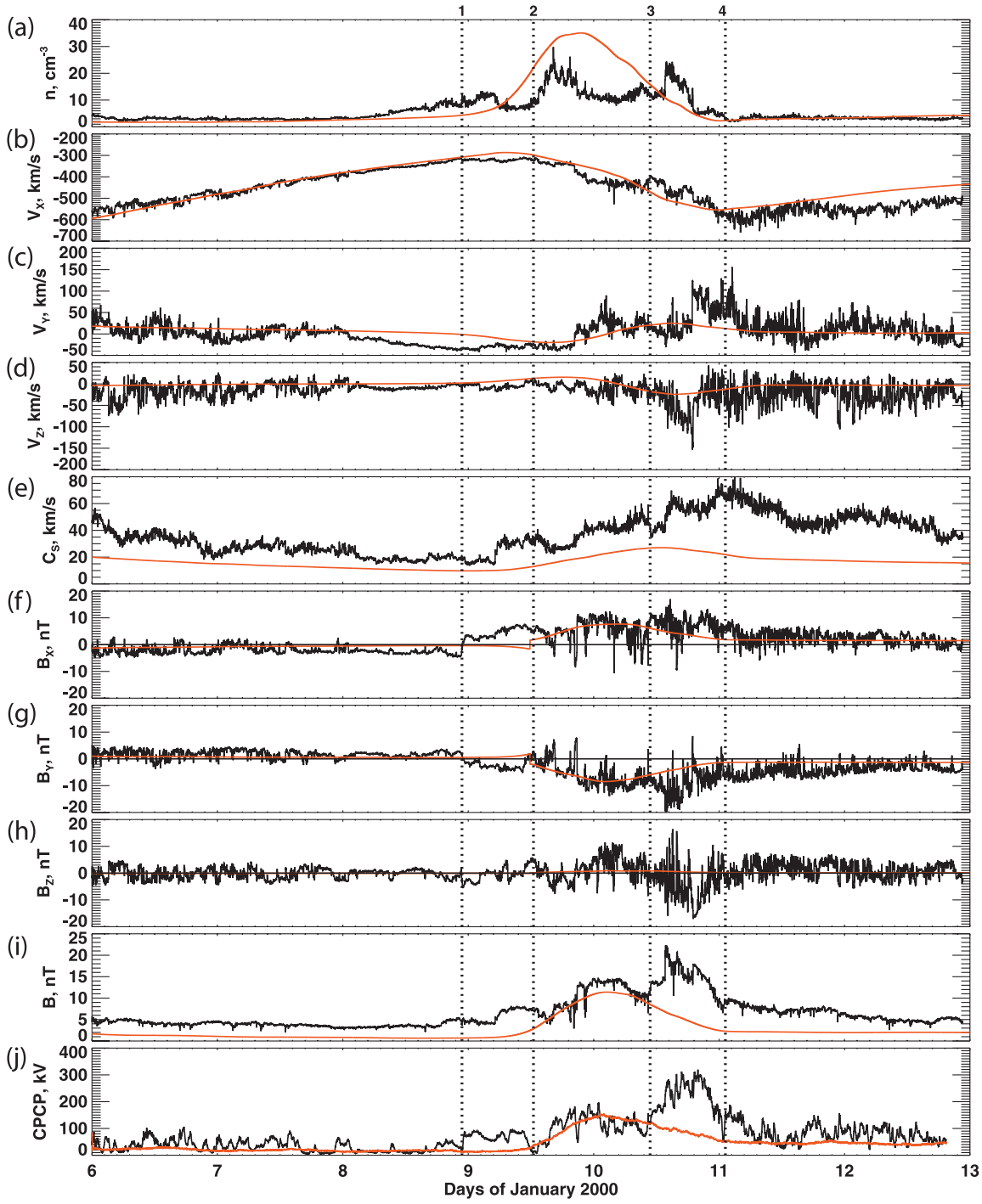

Figure 5. (a–i) Solar wind parameters are observed by the ACE spacecraft (black traces) and simulated by the CORHEL model (red traces) in GSE coordinates. (j) Cross–polar cap potential evolution simulated by the LFM model with the ACE input (black traces) and the CORHEL input (red traces). The two regions between the vertical lines 1–2 and 3–4, respectively, show intervals when the cross–polar cap potential evolution is not well captured by the LFM model driven by the CORHEL input (see text for details).

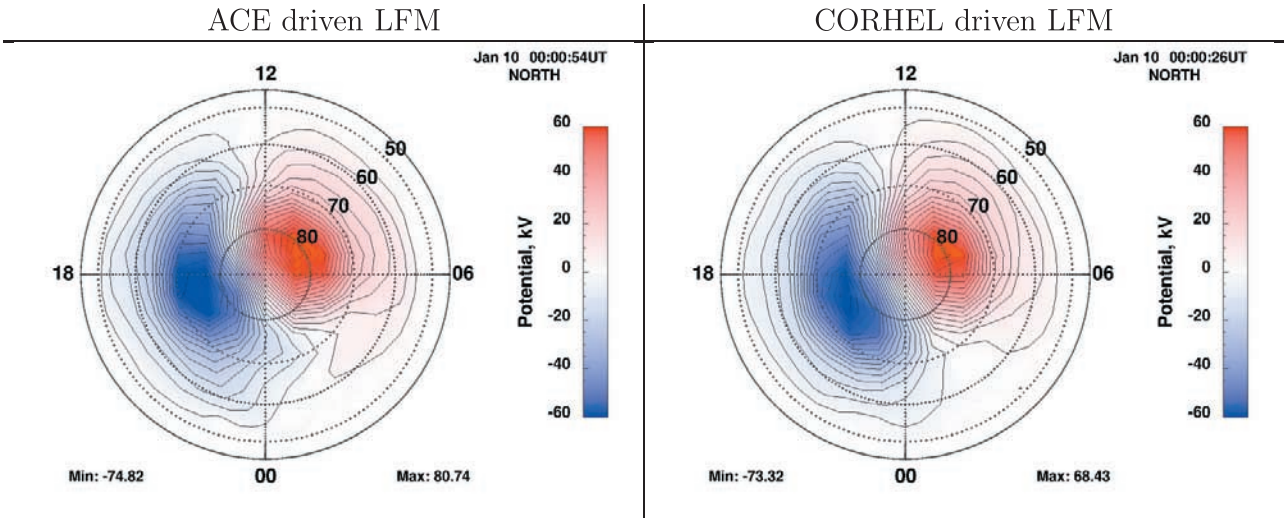

Figure 6. Northern hemisphere potential simulated by (left) the LFM model driven by the ACE spacecraft data and (right) the CORHEL model output at the peak of the negative B_y-driven interval.

[35] It is worth noting again that Figure 5j (the interval between vertical lines 2 and 3) and Figure 6 demonstrate very good agreement in prediction of the cross–polar cap potential between the stand-alone LFM model and the end-to-end simulation for a period as long as 1 d. This result emphasizes that even at this initial stage of developing end-to-end coupled models, in the presence of such restrictive factors as the stationarity of the heliospheric model or the lack of significant IMF B_z variations, it is already possible to obtain a sensible prediction of magnetospheric dynamics on a gross scale for a relatively long period of time.

5. Conclusion and Summary

[36] Development of coupled models of the Sun-Earth system is essential for prediction of space weather conditions in the near-Earth environment. There are many challenges that the modeling community faces, both fundamental and technical ones that prevent us presently from making reliable predictions of arbitrary conditions. Nevertheless, the simulations presented in this paper demonstrate that some promising results can already be achieved, provided that favorable conditions exist in the heliosphere.

[37] To emphasize this point, we presented results of two end-to-end numerical studies using the CISM 1.0, CMIT 1.0, and stand-alone LFM models, simulating interactions of space plasmas from the corona of the Sun to the Earth's ionosphere. In these studies we utilized observations of the solar wind and the IMF at the L1 point as well as the output from the coupled model of the solar corona and the solar wind, CORHEL, to drive the global coupled model of the magnetosphere-ionosphere, CMIT 1.0, and the stand-alone LFM model.

[38] We selected two 6- to 7-d intervals belonging to two different Carrington rotations, during which the HCS exhibited different geometry, posing different conditions for modeling by the heliospheric model, CORHEL. In the first simulation, during CR 1906, the flatness of the HCS had the result that the L1 point skimmed the current sheet, making it especially difficult for the model to predict an HCS crossing. In the absence of CMEs or CIRs in the simulation, a distinct time-dependent structure of the solar wind can only be observed by an L1 monitor if it crosses the HCS. In this first simulation, such a crossing did not occur, which led to an essentially trivial response of the magnetosphere-ionosphere system simulated by the CMIT 1.0 model. Because of this trivial response of the fully coupled end-to-end model, we concentrated on contrasting the results of CMIT 1.0 and LFM simulations, driven by the Wind spacecraft data, to each other as well as to the Weimer'05 model results, which allowed us to discuss effects of different ionospheric conductivity models on global MHD simulations of the magnetosphere during this relatively quiet period.

[39] The second selected interval (CR 1958) presented very different HCS conditions for CORHEL modeling. In this case, the distinct three-dimensional structure of the HCS allowed CORHEL to capture an HCS crossing quite well, which led to a significantly varying time series of simulated solar wind and IMF conditions at the L1 point for input into the LFM model. In this part of the study we concentrated on the magnetospheric response to features in the solar wind that were captured or not captured by the CORHEL model, and we were not interested in the effects of the ionospheric conductance. Therefore, for the magnetospheric part of the simulation, only the stand-alone LFM model was run, instead of the coupled CMIT 1.0 model. We found that periods of activity that were

driven by the B_y component of the IMF, captured by the CORHEL model, were reproduced quite accurately by the LFM model. As soon as the B_z IMF component turned southward for an extended period of time (not captured by the CORHEL model), the LFM model failed to respond, since the key component of the driver was absent. However, the agreement of the cross–polar cap potential, which we used as a global indicator of magnetospheric activity, and the corresponding ionospheric convection pattern during the well-reproduced periods was quite remarkable. This result demonstrates that even at these initial stages of developing fully coupled end-to-end models of the Sun-to-Earth space environment, when heliospheric models lack small-scale features crucial for driving the magnetosphere, i.e., IMF B_z variations, and large time-varying structures, i.e., CMEs, they can already produce reliable predictions of gross features of the magnetospheric dynamics in situations when the primary driver is well captured by the heliospheric model, i.e., B_y evolution at an HCS crossing.

[40] **Acknowledgments.** We are grateful to the model developers for providing the models used for validation: J. Linker and P. Riley (SAIC) for the MAS model, D. Odstrcil (CU) for ENLIL, and M. Wiltberger and W. Wang (NCAR HAO) for the CMIT model. C. Goodrich (Boston University) developed the code to couple the CORHEL and LFM simulation codes. We thank N. Ness (Bartol Research Institute) for the ACE magnetic field 16 s data and D. J. McComas (Southwest Research Institute) for the solar wind plasma data from the ACE SWEPAM instrument at 64 s resolution. Both data sets were obtained through the CDAWeb (http://cdaweb.gsfc.nasa.gov). We thank T. Guild (Aerospace Corporation) for providing stand-alone LFM simulation data for the CR 1906 simulation as well as for the solar wind input parameters for that interval. The computations were accomplished on the CISM IBM Power4 supercomputers located at Boston University and were supported by the BU SCV group. This research was supported by the National Science Foundation under agreement ATM-012950, which funds the CISM project of the STC program.

References

Bittencourt, J. A. (2004), *Fundamentals of Plasma Physics*, 3rd ed., p. 12, Springer, New York.

Burton, M. E., N. U. Crooker, G. L. Siscoe, and E. J. Smith (1994), A test of source-surface model predictions of heliospheric current sheet inclination, *J. Geophys. Res.*, *99*, 1–9.

Fedder, J. A., and J. G. Lyon (1995), The Earth's magnetosphere is 165 R_E long: Self-consistent currents, convection, magnetospheric structure, and processes for northward interplanetary magnetic field, *J. Geophys. Res.*, *100*, 3623–3636.

Fedder, J. A., J. G. Lyon, S. P. Slinker, and C. M. Mobarry (1995a), Topological structure of the magnetotail as function of interplanetary magnetic field direction, *J. Geophys. Res.*, *100*, 3613–3622.

Fedder, J. A., S. P. Slinker, J. G. Lyon, and R. D. Elphinstone (1995b), Global numerical simulation of the growth phase and the expansion onset for substorm observed by Viking, *J. Geophys. Res.*, *100*, 19,083–19,093.

Goodman, M. L. (1995), A three-dimensional, interative mapping procedure for the implementation of an ionosphere-magnetosphere anisotropic Ohm's law boundary condition in global magnetohydrodynamic simulations, *Ann. Geophys.*, *13*, 843–853.

Guild, T. B. (2007), Comparative studies of multiscale convective transport through the Earth's plasma sheet, Ph.D. thesis, Boston Univ., Boston, Mass.

Haaland, S. E., G. Paschmann, M. Förster, J. M. Quinn, R. B. Torbert, C. E. McIlwain, H. Vaith, P. A. Puhl-Quinn, and C. A. Kletzing (2007), High-latitude plasma convection from Cluster EDI measurements: Method and IMF-dependence, *Ann. Geophys.*, *25*, 239–253.

Lepping, R. P., and K. W. Behannon (1980), Magnetic field directional discontinuities: 1. Minimum variance errors, *J. Geophys. Res.*, *85*, 4695–4703.

Linker, J., Z. Mikic, D. A. Biesecker, R. J. Forsyth, W. E. G. A. J. Lazarus, A. Lecinski, P. Riley, A. Szabo, and B. Thompson (1999), Magnetohydrodynamic modeling of the solar corona during whole Sun month, *J. Geophys. Res.*, *104*, 9809–9830.

Lionello, R., J. A. Linker, and Z. Mikic (2001), Including the transition region in models of the large-scale solar corona, *Astrophys. J.*, *546*, 542–551.

Lotko, W. (2004), Inductive magnetosphere-ionosphere coupling, *J. Atmos. Sol. Terr. Phys.*, *66*, 1443–1456.

Luhmann, J. G., S. C. Solomon, J. A. Linker, J. G. Lyon, Z. Mikic, D. Odstrcil, W. Wang, and M. Wiltberger (2004), Coupled model simulation of a Sun-to-Earth space weather event, *J. Atmos. Terr. Phys.*, *66*, 1243–1256.

Lyon, J. G., J. A. Fedder, and C. M. Mobarry (2004), The Lyon-Fedder-Mobarry (LFM) global MHD magnetospheric simulation code, *J. Atmos. Sol. Terr. Phys.*, *66*, 1333–1350.

Mallinckrodt, A. J., and C. W. Carlson (1978), Relations between transverse electric fields and field-aligned currents, *J. Geophys. Res.*, *83*, 1426–1432.

Merkin, V. G., G. Milikh, K. Papadopoulos, J. Lyon, Y. S. Dimant, A. S. Sharma, C. Goodrich, and M. Wiltberger (2005), Effect of anomalous electron heating on the transpolar potential in the LFM global MHD model, *Geophys. Res. Lett.*, *32*, L22101, doi:10.1029/2005GL023315.

Merkin, V. G., J. G. Lyon, B. J. Anderson, H. Korth, C. C. Goodrich, and K. Papadopoulos (2007), A global MHD simulation of an event with a quasi-steady northward IMF component, *Ann. Geophys.*, *25*, 1345–1358.

Mikic, Z., and J. Linker (1994), Disruption of coronal magnetic field arcades, *Astrophys. J.*, *430*, 898–912.

Mikic, Z., J. A. Linker, D. D. Schnack, R. Lionello, and A. Tarditi (1999), Magnetohydrodynamic modeling of the global solar corona, *Phys. Plasmas*, *6*, 2217–2224.

Odstrcil, D. (2003), Modeling 3-D solar wind structures, *Adv. Space Res.*, *32*, 497–506.

Odstrcil, D., V. Pizzo, J. A. Linker, P. Riley, R. Lionello, and Z. Mikic (2004), Initial coupling of coronal and heliospheric numerical magnetohydrodynamic codes, *J. Atmos. Sol. Terr. Phys.*, *66*, 1311–1320.

Owens, M. J., C. N. Arge, H. E. Spence, and A. Pembroke (2005), An event-based approach to validating solar wind speed predictions: High-speed enhancements in the Wang-Sheeley-Arge model, *J. Geophys. Res.*, *110*, A12105, doi:10.1029/2005JA011343.

Rich, F. J., and M. Hairston (1994), Large-scale convection patterns observed by DMSP, *J. Geophys. Res.*, *99*, 3827–3844.

Riley, P., J. A. Linker, and Z. Mikic (2001), An empirically-driven global MHD model of the solar corona and inner heliosphere, *J. Geophys. Res.*, *106*, 15,889–15,902.

Robinson, R. M., R. R. Vondrak, K. Miller, T. Babbs, and D. A. Hardy (1987), On calculating ionospheric conductivities from the flux and energy of precipitating electrons, *J. Geophys. Res.*, *92*, 2565–2569.

Roble, R. G., E. C. Ridley, A. D. Richmond, and R. E. Dickinson (1988), A coupled thermosphere/ionosphere general circulation model, *Geophys. Res. Lett.*, *15*, 1325–1328.

Spence, H., D. Baker, A. Burns, T. Guild, C.-L. Huang, G. Siscoe, and R. Weigel (2004), Center for Integrated Space Weather Modeling

metrics plan and initial model validation results, *J. Atmos. Sol. Terr. Phys.*, *66*, 1499–1507.

Toten, T. L., J. W. Freeman, and S. Arya (1995), An empirical determination of the polytropic index for the free-streaming solar wind using HELIOS 1 data, *J. Geophys. Res.*, *100*, 13–17.

Wang, W., T. L. Killeen, A. G. Burns, and R. G. Roble (1999), A high-resolution, three-dimensional, time-dependent, nested grid model of the coupled thermosphere-ionosphere, *J. Atmos. Sol. Terr. Phys.*, *61*, 385–397.

Wang, W., M. Wiltberger, A. G. Burns, S. C. Solomon, T. L. Killeen, N. Maruyama, and J. G. Lyon (2004), Initial results from the coupled magnetosphere-ionosphere-thermosphere model: Thermosphere-ionosphere responses, *J. Atmos. Sol. Terr. Phys.*, *66*, 1425.

Weimer, D. R. (2005a), Predicting surface geomagnetic variations using ionospheric electrodynamic models, *J. Geophys. Res.*, *110*, A12307, doi:10.1029/2005JA011270.

Weimer, D. R. (2005b), Improved ionospheric electrodynamic models and application to calculating Joule heating rates, *J. Geophys. Res.*, *110*, A05306, doi:10.1029/2004JA010884.

Wiltberger, M., W. Wang, A. G. Burns, S. C. Solomon, J. G. Lyon, and C. C. Goodrich (2004), Initial results from the coupled magnetosphere-ionosphere-thermosphere model: magnetospheric and ionospheric responses, *J. Atmos. Sol. Terr. Phys.*, *66*, 1411.

Winglee, R. M., D. Chua, M. Brittnacher, G. K. Parks, and G. Lu (2002), Global impact of ionospheric outflows on the dynamics of the magnetosphere and cross-polar cap potential, *J. Geophys. Res.*, *107*(A9), 1237, doi:10.1029/2001JA000214.

W. J. Hughes, V. G. Merkin, M. J. Owens, J. M. Quinn, and H. E. Spence, Center for Space Physics, Boston University, 725 Commonwealth Ave., Boston, MA 02215, USA. (vgm@bu.edu)